Supplementary Information (SI) for Journal of Materials Chemistry A.

Supporting Information

Experimental Section

Catalyst Preparation

n%ReO_2@TiO_2 (*n* = 0.1, 0.5, 1, 2 and 5) photocatalysts were prepared by impregnation. Certain amount of NH_4ReO_4 (HEOWNS, 99%) was dissolved in 20 mL deionized water. After adding 0.5 g TiO_2 (Macklin, 99.99%) into the Re-containing solution, the mixture was continuously stirred at 333 K for 4 h and then dry at 383 K overnight to remove the solvent. The collected powder was then calcined in air at 773 K for 4 h and reduced in 10 vol% H_2/Ar at 773 K for 3 h. The obtained photocatalysts were labeled as *n*%ReO_2@TiO_2. H_2-TiO_2 was prepared using the same method with that to prepare *n*%ReO_2@TiO_2 but without the addition of NH_4ReO_4.

Characterization

X-ray diffraction (XRD) analyses were performed on a Shimadzu XRD-6000 diffractometer with Cu Kα radiation. The X-ray tube was operated at 40 kV and 40 mA. All diffraction patterns were recorded in a range from 10° to 80° at a scanning rate of $5°\cdot min^{-1}$. N_2 adsorption-desorption isotherms were obtained at 77 K on a Micromeritics ASAP 2460 analyzer. Specific surface area is determined by using the Brunauer Emmett-Teller (BET) method at 77.3 K, respectively. Steady state photoluminescence (PL) emission spectra were detected by an Edinburgh FLS980 PL spectrometer with an excitation wavelength of 365 nm. Time-resolved fluorescence decay spectra were recorded with the time-correlated single photo counting mode. The average fluorescence lifetime (Δ_{avg}) was determined based on the fitting of double exponential function. X-ray photoelectron spectroscopy (XPS) was conducted in a Shimadzu Axis Supra+ spectrometer equipped with a monochromatic Al Kα (1486.6 eV) radiation generated from the electron beam operated at 150 W. The spectra were referenced to the C 1s peak at 284.8 eV. Electron paramagnetic resonance (EPR) spectroscopy was obtained on a Bruker E500 electron magnetic resonance spectrometer at room temperature.

Temperature-programmed desorption of oxygen (O_2-TPD) and methane (CH_4-TPD) was carried out in a Microtrac BELCat II chemisorption analyzer. Typically, 50 mg sample was loaded in a U-shaped quartz tube and pre-treated with flowing hydrogen (10 vol.%) at 773 K for 1 h. After cooling down to 293 K under argon flow, the sample was saturated with O_2 or CH_4 for 1 h and then purged with argon to remove the physically-adsorbed O_2 or CH_4. Lastly, the whole system was heated to 1073 K at a rate of 10 $K\cdot min^{-1}$.

Photocurrents were measured on a CHI760E electrochemical workstation in a Na_2SO_4 solution (0.1 M) using a 300 W Xe-lamp, with a constant potential of 0.2 V vs. reversible hydrogen electrode (RHE). Solution and light source used for measuring photocurrents are similar to those for photocatalytic reactions. The electrochemical workstation includes three electrodes. A Pt plate and an Ag/AgCl electrode were used as the counter electrode and reference electrode, respectively. For preparing the working electrode, with a surface area of 1.0 cm^2 exposed to electrolyte, 5 mg sample was first dispersed in the mixture of 900 μL ethanol and 100 μL 30 wt% Nafion solution under ultrasonication. Then, 100 μL suspension was dropped onto the electrode and dried at room temperature.

Computation Details

Density functional theory (DFT) calculations for cluster structures were performed by using Gaussian 16[1] and ORCA[2] programs. Initially, the B2GP-PLYP[3] function including DFT-D3 dispersion correction[4, 5] was used for structural optimization and frequency analysis. For geometry optimization, the def2-TZVP[6, 7] basis set was employed for all atoms. More accurate single-point energies were obtained at DLPNO-CCSD(T)/def2-TZVPP level of theory. Stationary points were optimized without symmetry constraint, and their nature was confirmed by vibrational frequency analysis. Natural bond orbital (NBO)[8-13] were performed to obtain further information. The graphics were generated using Chemcraft program. Corresponding density of states (DOS) analysis were carried out with Multifwn[14] programs.

Oxygen adsorption energy (ΔE) for ReO_x^+ ($x = 0 - 3$) clusters is calculated as $\Delta E = E(ReO_x^+\cdots O_2) - E(ReO_x^+) - E(O_2)$, where $E(ReO_x^+)$ and $E(O_2)$ represents the energy of the ground state of ReO_x^+ and triplet oxygen ($^3O_2$).

Different components of the total interaction energy between ReO_x^+ (x = 0 - 3) clusters and O_2 were calculated at TPSSh[15]/def2-TZVP level of theory by using sobEDA[16]. The total interaction energy (ΔE_{tot}) is decomposed to electrostatic energy (ΔE_{ele}), exchange energy (ΔE_x), repulsion energy (ΔE_{rep}), orbital energy (ΔE_{orb}), DFT correlation energy (ΔE_{DFT}) and dispersion correction energy (ΔE_{dc}), and coulomb correlation energy (ΔE_c) is defined as the sum of DFT correlation energy and coulomb correlation energy.

Density functional theory (DFT) calculations for condensed structures were performed using package VASP5.4.1.[17, 18] The generalized gradient approximation functional Perdew-Burke-Ernzerhof (PBE) was used for the exchange correlation functional, with the projected augmented wave (PAW) pseudopotential basis set and a cutoff energy of 450 eV.[19, 20] The van der Waals interactions were considered using the DFT-D3 empirical correction.[5] The electronic energy was considered self-consistent when the energy change was smaller than 10^{-5} eV. A geometry optimization was considered convergent when the energy change was smaller than 0.02 eV $Å^{-1}$. The lattice differences between the heterostructures are within 5%. Thermodynamic Gibbs free energy corrections and density of states (DOS) analysis were carried out with the aid of the VASPKIT 1.2.1 tool package.[21] The Brillouin zone integral uses the surfaces structures of 2×2×1 Monkhorst-Pack K-point sampling for structure. The cutoff energy and K-point were selected based on convergence tests. The Gibbs free energy of the reaction intermediates was calculated using the computational hydrogen electrode model, as shown below:

$$G = E_{DFT} + ZPE - TS$$

Where E is the energy obtained from DFT calculations, ZPE is the zero-point energy of the material, S is the entropy of the adsorbate, and T is the thermodynamic temperature (298.15K).

Photocatalytic measurements

The photocatalytic methane oxidation reaction tests were conducted in a 250 mL stainless steel autoclave equipped with two sapphire windows to allow light irradiation. Typically, 10 mg catalyst was dispersed in 100 mL water by ultrasonication for 5 min. Then, the mixture was added into the autoclave, and the temperature was set at 298

K. After sealing and purging with ultrapure O_2 (99.999 vol.%) for 20 min, 1 bar O_2 (purity, 99.999%) and 19 bar CH_4 (purity, 99.999%) were flowed into the autoclave. Subsequently, the solution was stirred at 800 rpm and a 300 W Xe lamp was used as the light source. The autoclave is equipped with a temperature probe and a pressure probe to measure liquid temperature and gas pressure respectively. During the reaction process, the temperature of the liquid solution was maintained at 25 ± 2 °C by turning on the heat and fan at the same time. After the reaction, the autoclave was cooled in an ice bath to a temperature below 283 K. Then the gas and liquid product were collected by bags and vacuum filtration, respectively.

AQE was then measured. In the experiment, 10mg 1.0%ReO_2@TiO_2 photocatalyst was first dispersed in 100 ml distilled water. Then the suspension was stirred and purged with ultrapure O_2 for 20 min. After flowing 1bar O_2 and 19 bar CH_4 into the reactor, the reaction was conducted for 1h with a Xe lamp as the light source equipped with a 365 nm bandpass filter. Light intensity was measured as 10.0 mW·cm^{-2} by the light intensity meter (TM-207, Tenmars Electronics Co., Ltd).

$$AQE = \frac{R(electron)N_A}{ISt/E_\lambda} \times 100\%$$

$$E_\lambda = \frac{hc}{\lambda}$$

Where NA, I, S and t represent the Avogadro's constant, light intensity irradiated on the sample (10.0 mW·cm^{-2}), irradiation area (12.56 cm^{-2}) and reaction time (1 h), respectively; h, c and λ represent Planck's constant, the speed and wavelength of light, and then the value of E_λ is 5.4 × 10^{-19} J.

R(electron) stands for the number of electrons engaged in the formation of products.

$$O_2 \overset{-(2e^- + 2H^+)}{\rightarrow} \cdot OH$$

$$O_2 \overset{-(e^- + H^+)}{\rightarrow} \cdot OOH$$

$$CH_4 + \ \cdot OH \rightarrow \ \cdot CH_3 + H_2O$$

$$\cdot CH_3 + \ \cdot OOH \rightarrow CH_3OOH \rightarrow HCHO \rightarrow HCOOH$$

$$\cdot CH_3 + \ \cdot OOH \rightarrow CH_3OOH \rightarrow CH_3OH$$

As shown in the above equations, the formation of CH_3OOH, CH_3OH, HCHO and

HCOOH needed 3, 5, 3 and 5 electrons, respectively. The as-produced CH3OOH, CH3OH, HCHO and HCOOH were 4.3, 1.2, 6.6 and 0.2 μmol, respectively. Therefore, AQE = (4.3 μmol × 3 + 1.2 μmol × 5 + 6.6 μmo l× 3 + 0.2 μmol × 5) × 6.02 × 10^{23} mol^{-1} × 100% / (10.0 $mW·cm^{-2}$ × 12.56 cm^2 × 1 × 3600s / 5.4 × 10^{-19} J) = 2.85%.

For isotopic labeling experiments, 10 mg 1.0%ReO_2@TiO_2 photocatalyst was dispersed in 4 mL $H_2{}^{16}O$ or $H_2{}^{18}O$. After the reactor being degassed for 20 min, 1 bar $^{18}O_2$ or $^{16}O_2$ and 9 bar CH_4 were injected into the reactor. After reacting for 4 h, the suspension was filtered and then the solvent was analyzed by GC-MS (Agilent 8890).

Analysis of Products

The concentrations of gas products were analyzed by gas chromatograph (GC, FuLi GC9790Plus) equipped with two flame ionization detectors (FID) and a thermal conductivity detector (TCD) with TDX-01 column. The temperature of the column box was maintained at 80 °C and the temperature of the TCD detector was set to 130 °C. The quantitative ring volume was 1 mL. The amounts of gas products were calculated by multiplying their concentrations by the volume (150 mL, under the condition of 1 bar O_2 and 19 bar CH_4).

The liquid product was analyzed by nuclear magnetic resonance spectroscopy (NMR) and the colorimetric method[22]. The concentration of CH_3OH, CH_3OOH and HCOOH in the liquid was quantified by ^1H NMR (Bruker AVANCE NE0 500). Typically, 600 μL liquid product was mixed with 0.1 mL internal standard solution consisted of 0.2 μL internal standard dimethyl sulfoxide (DMSO, Aladdin, 99.99%) and 5 mL D_2O. The concentration of liquid product HCHO was quantified by the colorimetric method.37 Typically, 100 mL of reagent aqueous solution was first prepared by dissolving 15 g of ammonium acetate, 0.3 mL of acetic acid, and 0.2 mL of pentane-2,4-dione in water. Then, 0.5 mL of liquid product was mixed with 2.0 mL of water and 0.5 mL of reagent solution. The mixed solution was maintained at 35 °C in a water bath and measured by UV−vis absorption spectroscopy until the absorption intensity at 412 nm did not further increase. The concentration of HCHO in the liquid product was determined by the standard curve (Figure S1).

DMPO was used as the spin-trapping agent to monitor the reactive species including

·OOH and ·OH radicals. For ·OOH radical detection, 10 mg pure TiO_2 or 1.0%ReO_2@TiO_2 photocatalyst was dispersed into 1 mL DMPO/methanol solution. After purging with ultrapure O_2 (99.999 vol.%) for 20 min, in situ EPR spectra were collected after 15 min light irradiation. For ·OH radical detection, 10 mg pure TiO_2 or 1.0%ReO_2@TiO_2 photocatalyst was dispersed in 1 mL aqueous DMPO solution. After purging with ultrapure O_2 (99.999 vol.%) or Ar (99.999 vol.%) for 20 min, in situ EPR spectra were collected after 15 min light irradiation.

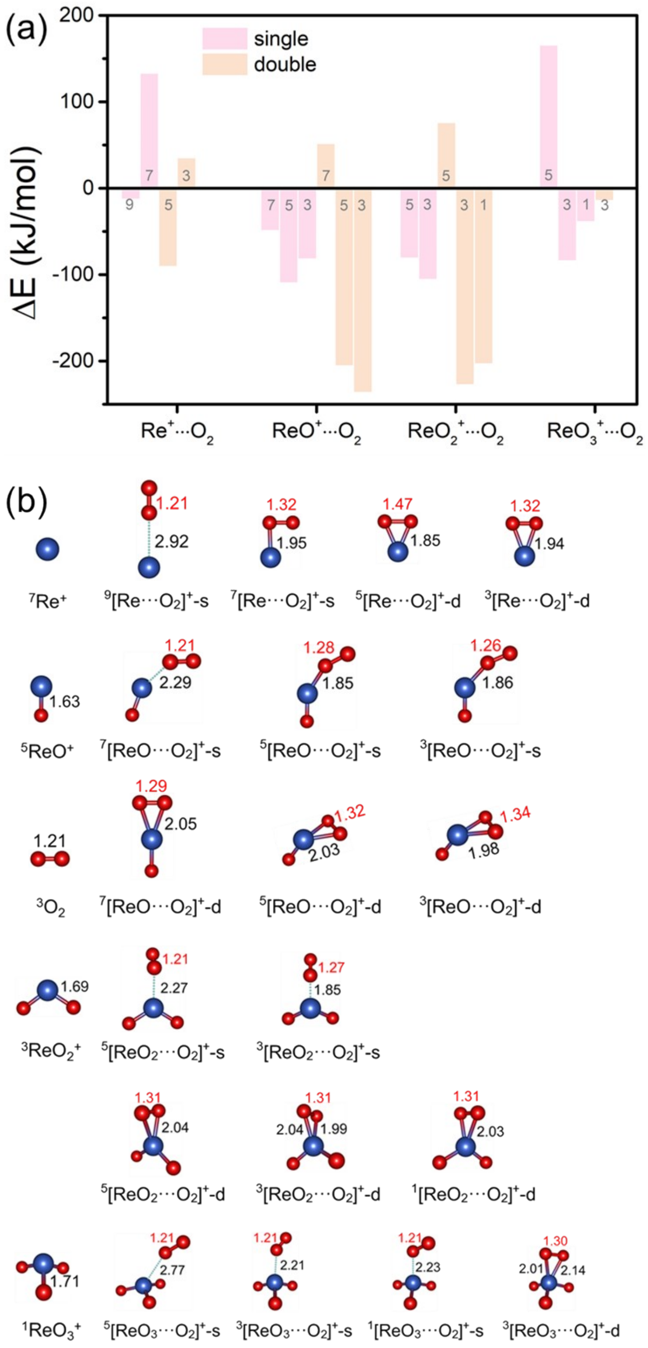

Figure S1. (a) O_2 adsorption energy for ReO_x^+ (x = 0 - 3) clusters as calculated at the DLPNO-CCSD(T)/def2-TZVPP//B2GP-PLYP/def2-TZVP level of theory. Two adsorption modes of O_2 were considered: single (s) - adsorption by a single oxygen atom and double (d)- simultaneous adsorption of two oxygen atoms. The grey number represents the spin state of the complex. (b) The optimized structures of ReO_x^+ (x = 0 - 3) and corresponding structures after O_2 adsorption as calculated at the DLPNO-CCSD(T)/def2-TZVPP//B2GP-PLYP/def2-TZVP level of theory. Bond length are given in Å. Charges are omitted for the sake of clarity.

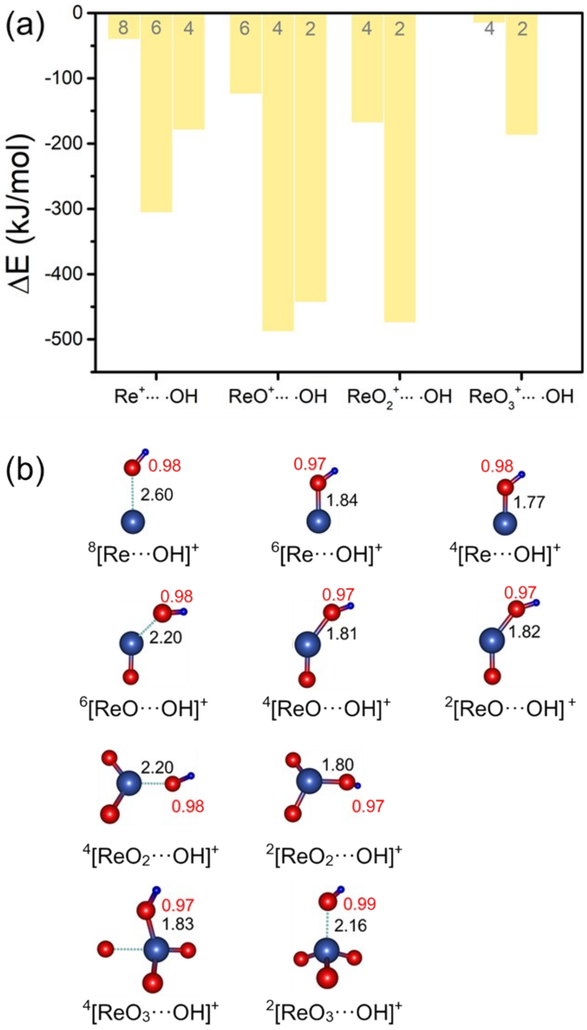

Figure S2. (a) ·OH adsorption energy for ReO_x^+ (x = 0 - 3) clusters as calculated at the DLPNO-CCSD(T)/def2-TZVPP//B2GP-PLYP/def2-TZVP level of theory. The grey number represents the spin state of the complex. (b) The optimized structures of ReO_x^+ (x = 0 - 3) and corresponding structures after ·OH adsorption as calculated at the DLPNO-CCSD(T)/def2-TZVPP//B2GP-PLYP/def2-TZVP level of theory. Bond length are given in Å. Charges are omitted for the sake of clarity.

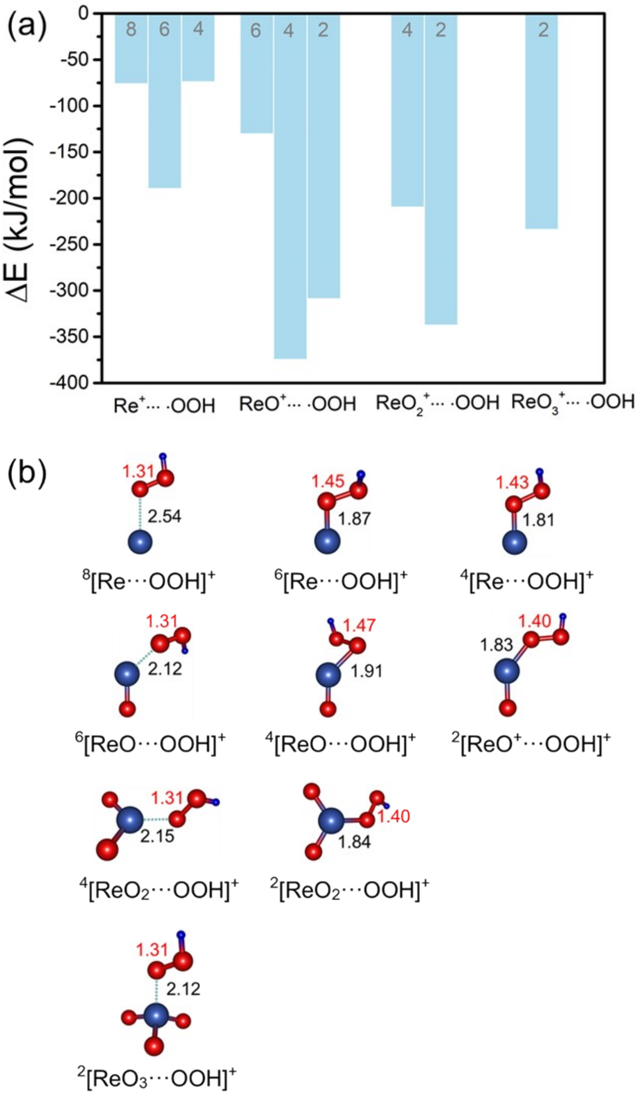

Figure S3. (a) ·OOH adsorption energy for ReO$_x^+$ (x = 0 - 3) clusters as calculated at the DLPNO-CCSD(T)/def2-TZVPP//B2GP-PLYP/def2-TZVP level of theory. The grey number represents the spin state of the complex. (b) The optimized structures of ReO$_x^+$ (x = 0 - 3) and corresponding structures after ·OOH adsorption as calculated at the DLPNO-CCSD(T)/def2-TZVPP//B2GP-PLYP/def2-TZVP level of theory. Bond length are given in Å. Charges are omitted for the sake of clarity.

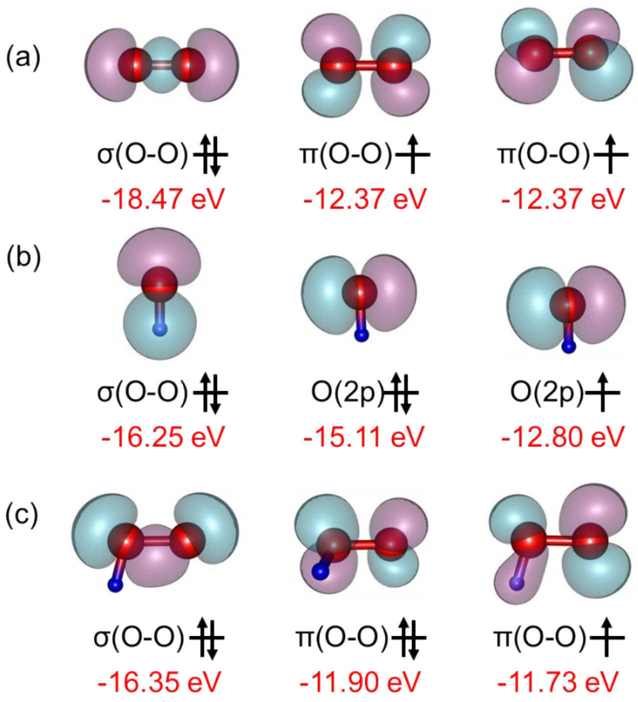

Figure S4. Frontier molecular orbital analysis of O_2, ·OH and ·OOH.

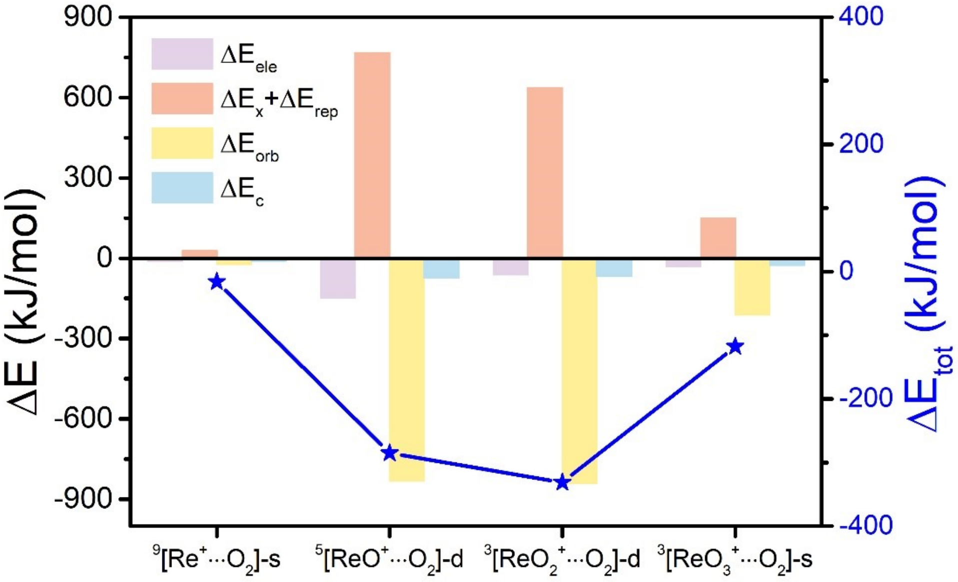

Figure S5. Decomposition of interaction energies (kJ/mol) in the $ReO_x^+\cdots O_2$ (x = 0 – 3) structures as calculated at the TPSSh-D3(BJ)/def2-TZVP level of theory.

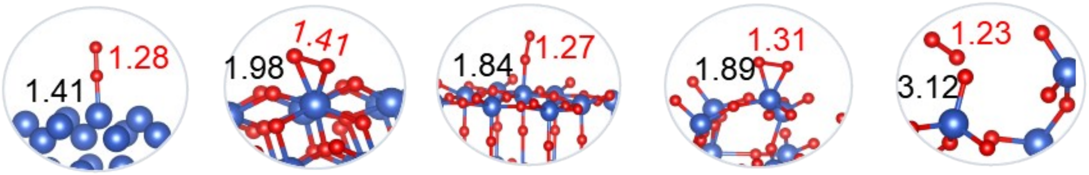

Re-O_2 ReO$_2$-O_2 ReO$_3$-O_2 Re$_2$O$_7$-O_2 Re$_2$O$_9$-O_2

Figure S6. Optimized geometries of O2 adsorbed on Re, ReO_2, ReO_3, Re_2O_7 and Re_2O_9 surface. Bond length are given in Å.

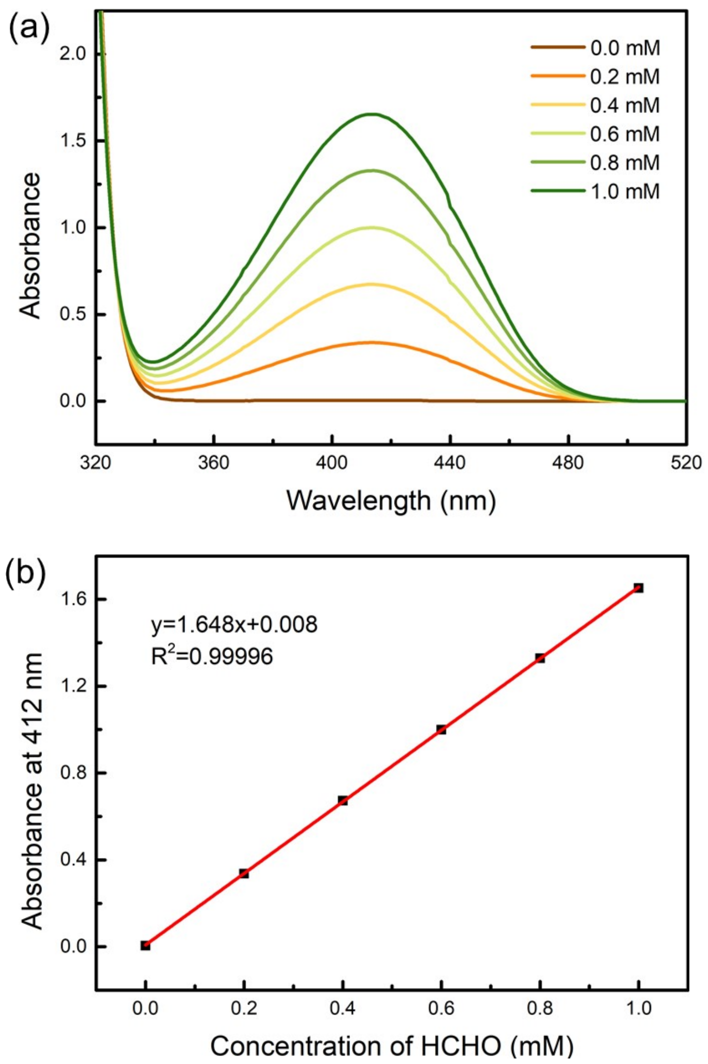

Figure S7. (a) UV-vis absorption spectra of formaldehyde standard solution; (b) Calibration curve for quantification of HCHO by colorimetric method.

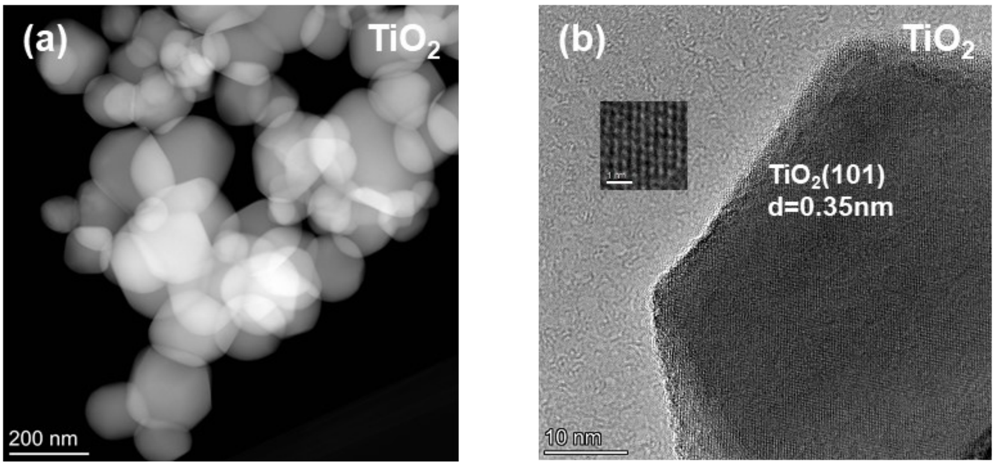

Figure S8. (a) HAADF-STEM and (b) TEM imagines of TiO_2 support.

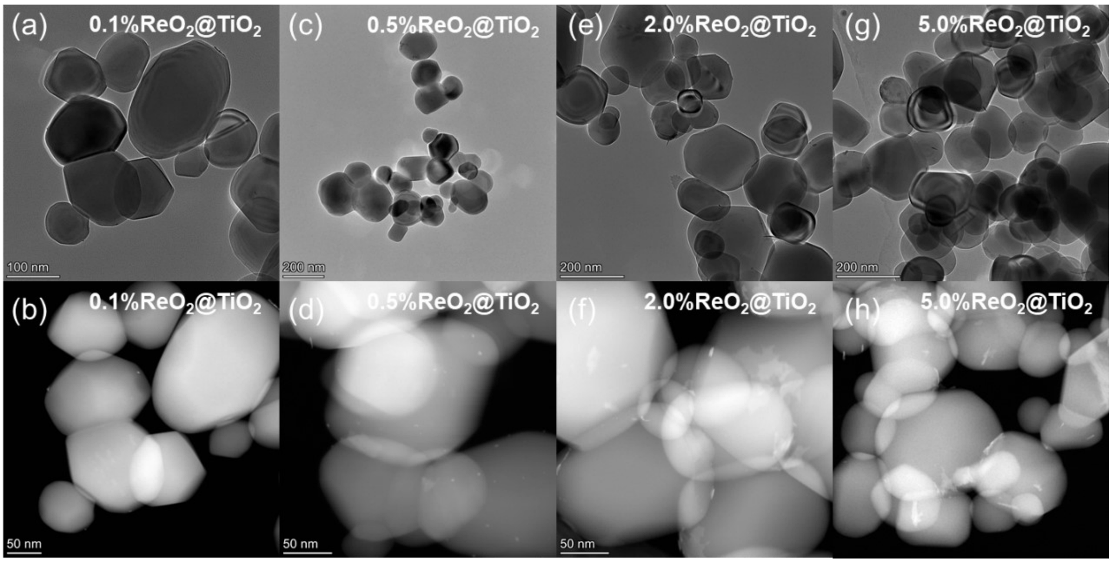

Figure S9. TEM and HAADF-STEM images of (a-b) 0.1%ReO_2@TiO_2; (c-d) 0.5%ReO_2@TiO_2; (e-f) 2.0%ReO_2@TiO_2; (g-h) 5.0%ReO_2@TiO_2.

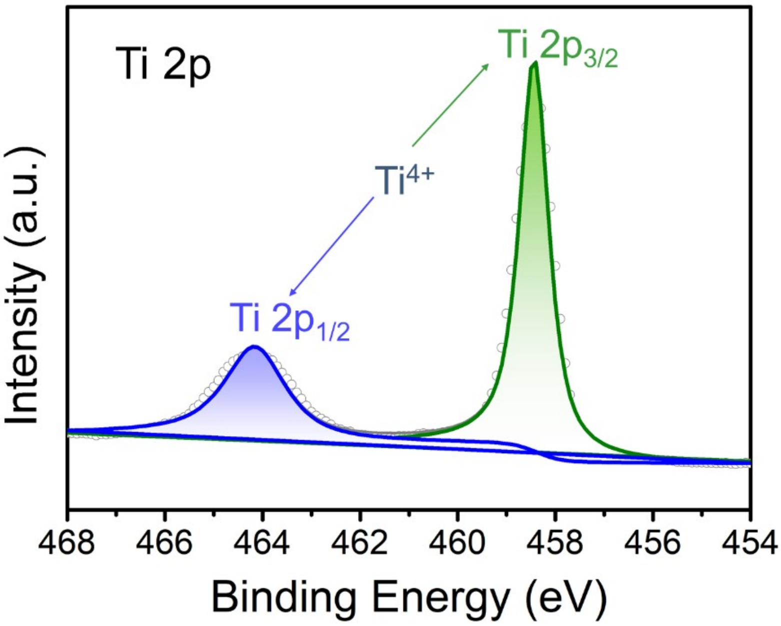

Figure S10. Ti 2p for 1.0%ReO_2@TiO_2.

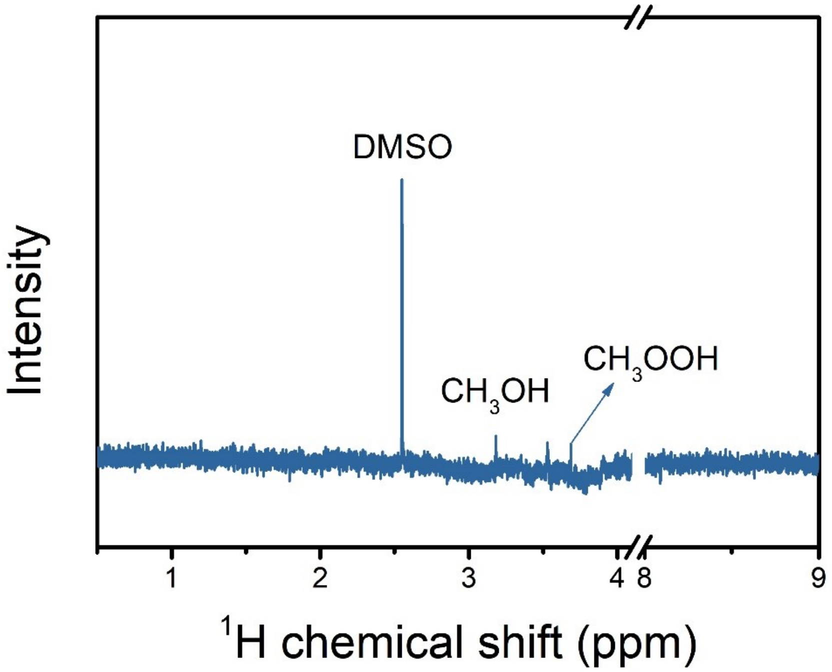

Figure S11. ^{1}H-NMR spectra of liquid products after photocatalytic oxidation of methane for 1h over pure TiO_2.

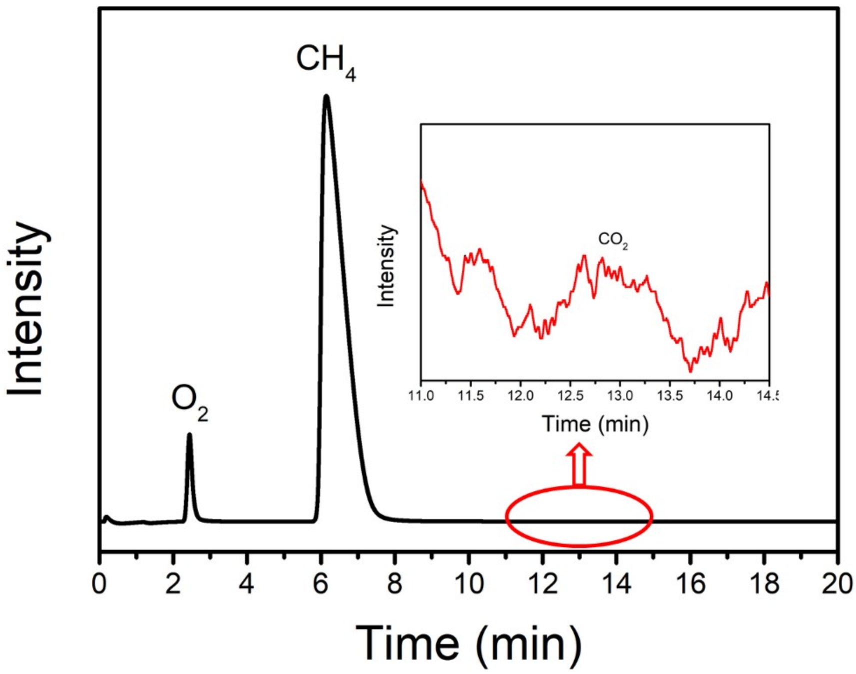

Figure S12. Typic spectra of gas products after photocatalytic oxidation of methane by GC with TCD detector. Reactant O_2, CH_4 and product CO_2 were detected.

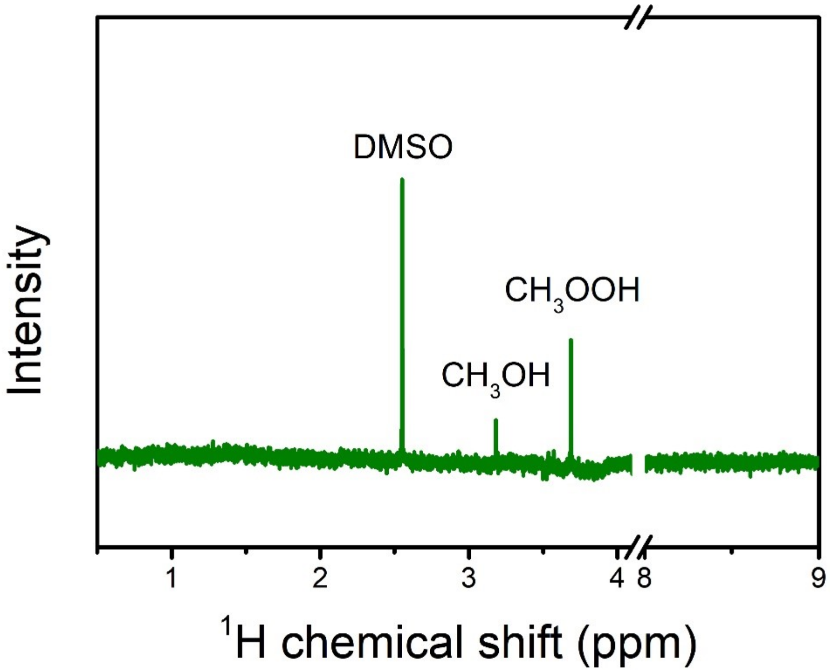

Figure S13. ^{1}H-NMR spectra of liquid products after photocatalytic oxidation of methane for 1h over H_2-TiO_2.

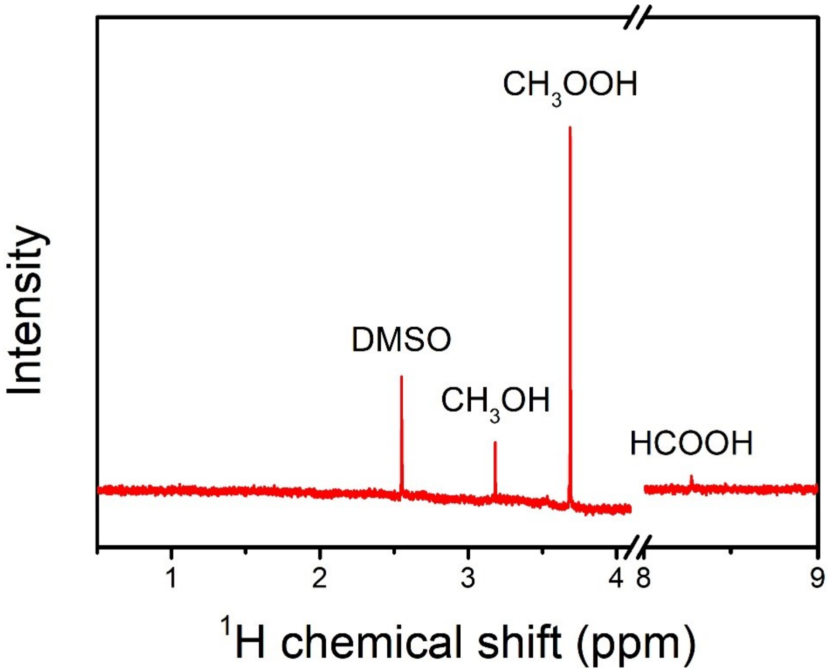

Figure S14. ^{1}H-NMR spectra of liquid products after photocatalytic oxidation of methane for 1h over 1.0%ReO_2@TiO_2.

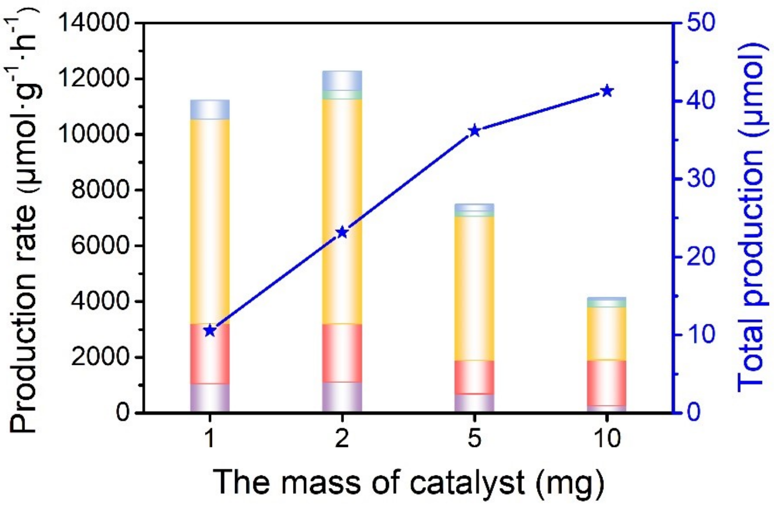

Figure S15. Production and total production of oxygenates obtained at different mass of 1.0%ReO_2@TiO_2 photocatalysts with 1 bar O_2 + 19 bar CH_4 in 100 ml deionized water under Xe light irradiation.

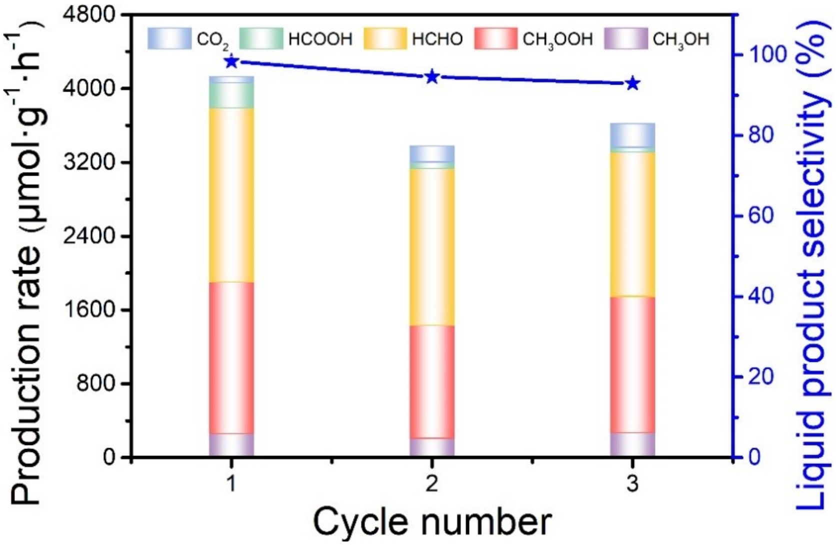

Figure S16. Product yields and liquid product selectivity over 10 mg 1.0%ReO_2@TiO_2 catalyst with 1 bar O_2 + 19 bar CH_4 in 100 ml deionized water under Xe light irradiation during the cycle experiments.

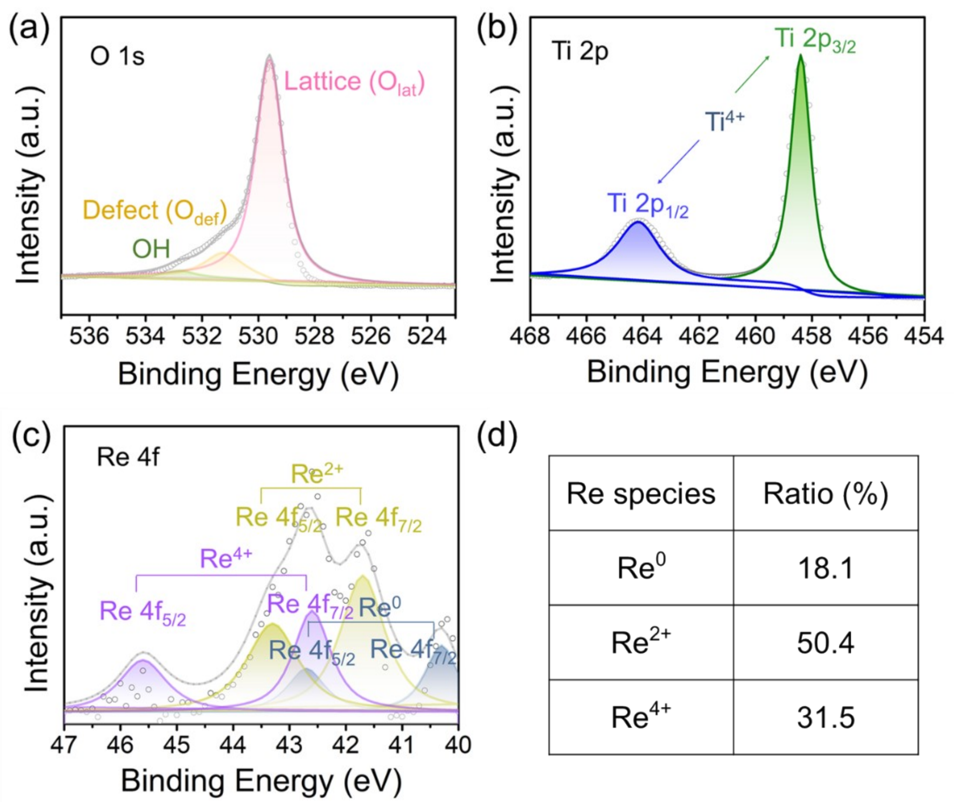

Re species	Ratio (%)
Re^{0}	18.1
Re^{2+}	50.4
Re^{4+}	31.5

Figure S17. XPS spectra of (a) O 1s, (b) Ti 2p, (c) Re 4f and (d) the composition of Re species for 1.0%ReO_x@TiO_2 catalyst after the cycling test experimrnt.

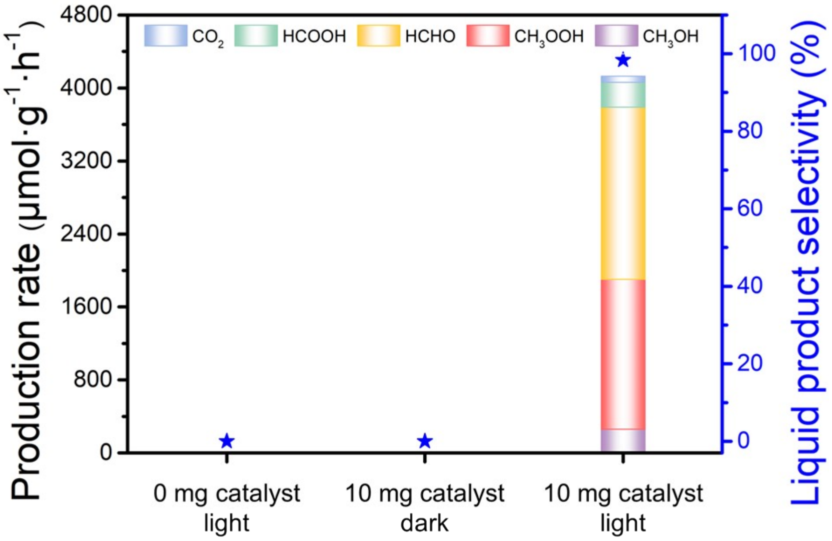

Figure S18. Product yields and liquid product selectivity at different reaction conditions: 0 mg catalyst under Xe light irradiation; 10 mg 1.0%ReO_2@TiO_2 catalyst under dark; 10 mg 1.0%ReO_2@TiO_2 catalyst under Xe light irradiation; 1 bar O_2, 19 bar CH_4 and 100 ml deionized water were used in the control reaction.

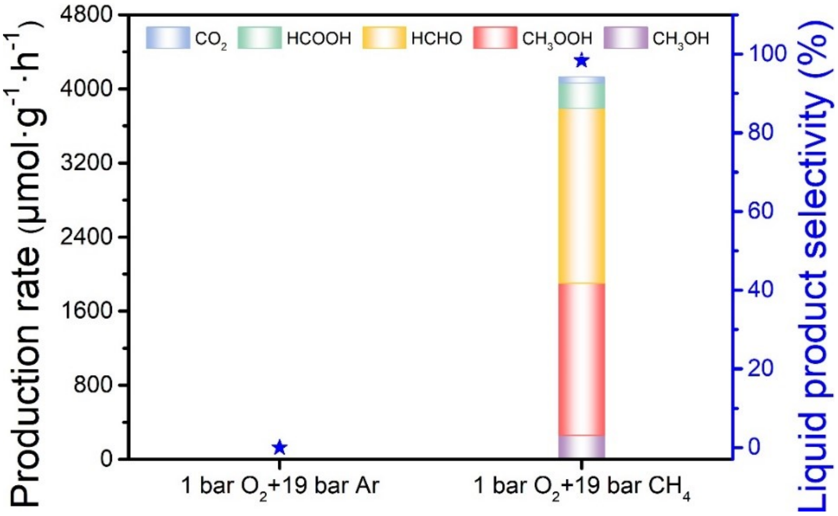

Figure S19. Product yields and liquid product selectivity over 10 mg 1.0%ReO_2@TiO_2 catalyst with 1 bar O_2 + 19 bar Ar or 1 bar O_2 + 19 bar CH_4 in 100 ml deionized water under Xe light irradiation, respectively.

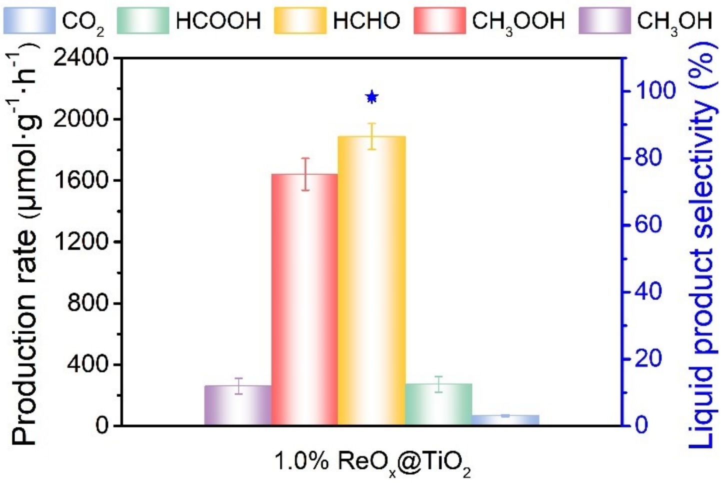

Figure S20. Error analysis of product yields and liquid product selectivity over 10 mg 1.0%ReO_2@TiO_2 catalyst for three different experiments with 1 bar O_2 + 19 bar CH_4 in 100 ml deionized water under Xe light irradiation.

Table S1. NBO charge and spin density of Re and O atoms for O_2 and ReO_x^+ (x = 0 - 3) clusters.

	NBO charge				spin density			
	Re	O_1	O_2	O_3	Re	O_1	O_2	O_3
$^3O_2$		0	0			1	1	
$^7Re^+$	1				6			
$^5ReO^+$	1.483	-0.483			4.271	-0.271		
$^3ReO_2^+$	1.958	-0.479	-0.479		1.945	0.028	0.028	
$^1ReO_3^+$	2.091	-0.364	-0.364	-0.364				

Table S2. The distance of Re-O and Re-Re in Re, ReO_2, ReO_3, Re_2O_7, Re_2O_9 structures.

Distance(Å)	Re-O	Re-Re
Re	-	0
ReO_2	2.02	3.90
ReO_3	1.90	3.70
Re_2O_7	1.80	3.30
Re_2O_9	1.90	3.70

Table S3. BET surface area of TiO_2, 0.1%ReO_2@TiO_2, 0.5%ReO_2@TiO_2, 1.0%ReO_2@TiO_2, 2.0%ReO_2@TiO_2 and 5.0%ReO_2@TiO_2.

Sample	BET surface area ($m^2 \cdot g^{-1}$)
TiO_2	8.7691
0.1%ReO_2@TiO_2	9.3618
0.5%ReO_2@TiO_2	8.9978
1.0%ReO_2@TiO_2	9.2248
2.0%ReO_2@TiO_2	8.1829
5.0%ReO_2@TiO_2	9.6192

Table S4. The comparison of liquid oxygenates yield and selectivity over 1.0%ReO_2@TiO_2 with other reported photocatalysts. All yields are converted to μmol·g^{-1}·h^{-1}.

photocatalyst	oxidant	reaction conditions	liquid product (μmol·g^{-1}·h^{-1})	Selectivity (%)	Ref
1.0%ReO_2@TiO_2	O_2	19 bar CH_4, 1 bar O_2,10mg, 1h reaction time, 25 ℃	4061.7	98.4	This work
1.0%ReO_2@TiO_2	O_2	19 bar CH_4, 1 bar O_2, 2mg, 1h reaction time, 25 ℃	12260.9	94.5	This work
Au/CoO_x/TiO_2	O_2	20 bar CH_4, 1 bar O_2, 2 h reaction time, 25 ℃	2540	95	23
$Au_{0.75}$/ZnOPd1-ZSM-5	O_2	15 bar CH_4, 5 bar O_2, 2 h reaction time, 25 ℃	1371	99.1	24
Au_{NPS}/In_2O_3	O_2	20 bar CH_4, 10 bar O_2, 3 h reaction time, 25 ℃	2066.7	91.05	25
Pd-def-In_2O_3	O_2	19 bar CH_4, 1 bar O_2, 3 h reaction time, 25 ℃	2996.7	99.4	26
2.1%Ag/TiO_2(101)	O_2	20 bar CH_4, 1 bar O_2, 2h reaction time, 25 ℃	4035	84.6	27
Cu_2@C_3N_4	O_2	1 bar CH_4, 1 bar O_2, 30 bar total pressure,	873.95	98.9	28
ZnO(Zni)-350	O_2	19 bar CH_4, 1 bar O_2, 2h reaction time, 30 ℃	3041	98.6	29
Pd_1-ZSM-5	H_2O_2 + CO	20 bar CH_4, 20 bar CO, 15 mL 0.6M H_2O_2, 0.5 h reaction time, 25 ℃	1236	100	30
0.33 wt% FeO_x/TiO_2	H_2O_2	0.2 bar CH_4, 4 mL 30 wt% H_2O_2,3 h reaction time, 25℃	760	97	31
TiO_2-C_3N_4	H_2O_2 + O_2	8%CH_4, 4% O_2, 20mL 1M H_2O_2, 25℃	696.3	97.0	32

Reference

1. Gaussian 16, R. A., M. J. Frisch, G. W. Trucks, H. B. Schlegel, G. E. Scuseria, M. A. Robb, J. R. Cheeseman, G. Scalmani, V. Barone, G. A. Petersson, H. Nakatsuji, X. Li, M. Caricato, A. V. Marenich, J. Bloino, B. G. Janesko, R. Gomperts, B. Mennucci, H. P. Hratchian, J. V. Ortiz, A. F. Izmaylov, J. L. Sonnenberg, D. Williams-Young, F. Ding, F. Lipparini, F. Egidi, J. Goings, B. Peng, A. Petrone, T. Henderson, D. Ranasinghe, V. G. Zakrzewski, J. Gao, N. Rega, G. Zheng, W. Liang, M. Hada, M. Ehara, K. Toyota, R. Fukuda, J. Hasegawa, M. Ishida, T. Nakajima, Y. Honda, O. Kitao, H. Nakai, T. Vreven, K. Throssell, J. A. Montgomery, Jr., J. E. Peralta, F. Ogliaro, M. J. Bearpark, J. J. Heyd, E. N. Brothers, K. N. Kudin, V. N. Staroverov, T. A. Keith, R. Kobayashi, J. Normand, K. Raghavachari, A. P. Rendell, J. C. Burant, S. S. Iyengar, J. Tomasi, M. Cossi, J. M. Millam, M. Klene, C. Adamo, R. Cammi, J. W. Ochterski, R. L. Martin, K. Morokuma, O. Farkas, J. B. Foresman, and D. J. Fox, Gaussian, Inc., Wallingford CT, 2016.
2. Neese, F., The ORCA Program System. *WIREs Comput. Mol. Sci.* **2012,** *2* (1), 73-78.
3. Karton, A.; Tarnopolsky, A.; Lamère, J.-F.; Schatz, G. C.; Martin, J. M. L., Highly Accurate First-Principles Benchmark Data Sets for the Parametrization and Validation of Density Functional and Other Approximate Methods. Derivation of a Robust, Generally Applicable, Double-Hybrid Functional for Thermochemistry and Thermochemical Kinetics. *J. Phys. Chem. A* **2008,** *112* (50), 12868-12886.
4. Grimme, S.; Antony, J.; Ehrlich, S.; Krieg, H., A Consistent and Accurate Ab Initio Parametrization of Density Functional Dispersion Correction (DFT-D) for the 94 Elements H-Pu. *J. Chem. Phys.* **2010,** *132* (15), 154104.
5. Grimme, S.; Ehrlich, S.; Goerigk, L., Effect of the Damping Function in Dispersion Corrected Density Functional Theory. *J. Comput. Chem.* **2011,** *32* (7), 1456-1465.
6. Andrae, D.; Häußermann, U.; Dolg, M.; Stoll, H.; Preuß, H., Energy-Adjustedab Initio Pseudopotentials for the Second and Third Row Transition Elements. *Theor. Chim. Acta* **1990,** 77 (2), 123-141.
7. Weigend, F.; Ahlrichs, R., Balanced Basis Sets of Split Valence, Triple Zeta Valence and Quadruple Zeta Valence Quality for H to Rn: Design and Assessment of Accuracy. Phys. Chem. Chem. Phys. **2005**, 7 (18), 3297-3305.
8. Foster, J. P.; Weinhold, F., Natural Hybrid Orbitals. J. Am. Chem. Soc. **1980**, 102 (24), 7211-7218.
9. Reed, A. E.; Weinhold, F., Natural Bond Orbital Analysis of Near-Hartree–Fock Water Dimer. *J. Chem. Phys.* **1983,** *78* (6), 4066-4073.
10. Reed, A. E.; Weinhold, F., Natural Localized Molecular Orbitals. *J. Chem. Phys.* **1985,** *83* (4), 1736-1740.
11. Reed, A. E.; Weinstock, R. B.; Weinhold, F., Natural Population Analysis. *J. Chem. Phys.* **1985,** *83* (2), 735-746.
12. Carpenter, J. E.; Weinhold, F., Analysis of the Geometry of the Hydroxymethyl Radical by The “Different Hybrids for Different Spins” Natural Bond Orbital Procedure. *J. Mol. Struct. THEOCHEM* **1988,** *169*, 41-62.
13. Reed, A. E.; Curtiss, L. A.; Weinhold, F., Intermolecular Interactions from A Natural Bond Orbital, Donor-Acceptor Viewpoint. *Chem. Rev.* **1988,** *88* (6), 899-926.
14. Lu, T.; Chen, F., Multiwfn: A Multifunctional Wavefunction Analyzer. *J. Comput. Chem.*

2012, *33* (5), 580-592.

15. Staroverov, V. N.; Scuseria, G. E.; Tao, J.; Perdew, J. P., Comparative Assessment of A New Nonempirical Density Functional: Molecules and Hydrogen-Bonded Complexes. *J. Chem. Phys.* **2003,** *119* (23), 12129-12137.

16. Lu, T.; Chen, Q., Simple, Efficient, and Universal Energy Decomposition Analysis Method Based on Dispersion-Corrected Density Functional Theory. *J. Phys.Chem. A* **2023,** *127* (33), 7023-7035.

17. Kresse, G.; Furthmüller, J., Efficient Iterative Schemes for Ab Initio Total-Energy Calculations using A Plane-Wave Basis Set. *Phys. Rev. B* **1996,** *54* (16), 11169-11186.

18. Kresse, G.; Furthmüller, J., Efficiency of Ab-Initio Total Energy Calculations for Metals and Semiconductors using A Plane-Wave Basis Set. *Comput. Mater. Sci.* **1996,** *6* (1), 15-50.

19. Perdew, J. P.; Burke, K.; Ernzerhof, M., Generalized Gradient Approximation Made Simple. *Phys. Rev. Lett.* **1996,** *77* (18), 3865.

20. Blöchl, P. E., Projector Augmented-Wave Method. *Physi. Rev. B* **1994,** *50* (24), 17953.

21. Wang, V.; Xu, N.; Liu, J. C.; Tang, G.; Geng, W. T., VASPKIT: A User-friendly Interface Facilitating High-throughput Computing and Analysis Using VASP Code. *Comput. Phys.* Commun. **2019,** *267*, 108033.

22. Browne, W. R.; Chen, J.; Draksharapu, A.; Gruden, M.; Stepanovic, S., A Non-Heme Iron Photocatalyst for Light-Driven Aerobic Oxidation of Methanol. *Angew. Chem. Int. Ed.* **2018**, 57 (12), 3207-3211.

23. Song, H.; Meng, X.; Wang, S.; Zhou, W.; Song, S.; Kako, T.; Ye, J., Selective Photo-oxidation of Methane to Methanol with Oxygen over Dual-Cocatalyst-Modified Titanium Dioxide. *ACS Catal.* **2020,** *10* (23), 14318-14326.

24. Zhou, W.; Qiu, X.; Jiang, Y.; Fan, Y.; Wei, S.; Han, D.; Niu, L.; Tang, Z., Highly Selective Aerobic Oxidation of Methane to Methanol over Gold Decorated Zinc Oxide via Photocatalysis. *J. Mater. Chem. A* **2020,** *8* (26), 13277-13284.

25. Jiang, Y.; Li, S.; Wang, S.; Zhang, Y.; Long, C.; Xie, J.; Fan, X.; Zhao, W.; Xu, P.; Fan, Y.; Cui, C.; Tang, Z., Enabling Specific Photocatalytic Methane Oxidation by Controlling Free Radical Type. *J. Am. Chem. Soc.* **2023,** *145* (4), 2698-2707.

26. Luo, L.; Fu, L.; Liu, H.; Xu, Y.; Xing, J.; Chang, C.-R.; Yang, D.-Y.; Tang, J., Synergy of Pd Atoms and Oxygen Vacancies on In2O3 for Methane Conversion under Visible Light. *Nat. Commun.* **2022,** *13* (1), 2930.

27. Feng, N.; Lin, H.; Song, H.; Yang, L.; Tang, D.; Deng, F.; Ye, J., Efficient and Selective Photocatalytic CH4 Conversion to CH3OH with O2 by Controlling Overoxidation on TiO2. *Nat. Commun.* **2021,** *12* (1), 4652.

28. Xie, P.; Ding, J.; Yao, Z.; Pu, T.; Zhang, P.; Huang, Z.; Wang, C.; Zhang, J.; Zecher-Freeman, N.; Zong, H.; Yuan, D.; Deng, S.; Shahbazian-Yassar, R.; Wang, C., Oxo Dicopper Anchored on Carbon Nitride for Selective Oxidation of Methane. *Nat. Commun.* **2022,** *13* (1), 1375.

29. Xiao, Z.; Wan, Z.; Zhang, J.; Jiang, J.; Li, D.; Shen, J.; Dai, W.; Li, Y.; Wang, X.; Zhang, Z., Interstitial Zinc Defects Enriched ZnO Tuning O2 Adsorption and Conversion Pathway for Superior Photocatalytic CH4 Oxygenation. *ACS Catal.* **2024,** *14* (12), 9104-9114.

30. Xu, W.; Liu, H.-X.; Hu, Y.; Wang, Z.; Huang, Z.-Q.; Huang, C.; Lin, J.; Chang, C.-R.; Wang, A.; Wang, X.; Zhang, T., Metal-Oxo Electronic Tuning via In Situ CO Decoration

for Promoting Methane Conversion to Oxygenates over Single-Atom Catalysts. *Angew. Chem. Int. Ed.* **2024,** *63* (16), e202315343.

31. Xie, J.; Jin, R.; Li, A.; Bi, Y.; Ruan, Q.; Deng, Y.; Zhang, Y.; Yao, S.; Sankar, G.; Ma, D.; Tang, J., Highly selective oxidation of methane to methanol at ambient conditions by titanium dioxide-supported iron species. *Nat. Catal.* **2018,** *1* (11), 889-896.

32. Sun, X.; Chen, X.; Fu, C.; Yu, Q.; Zheng, X.-S.; Fang, F.; Liu, Y.; Zhu, J.; Zhang, W.; Huang, W., Molecular oxygen enhances H2O2 utilization for the photocatalytic conversion of methane to liquid-phase oxygenates. *Nat. Commun.* **2022,** *13* (1), 6677.